



## Understanding the relative efficacies and versatile roles of 2D conductive nanosheets in hybrid-type photocatalyst



Suji Son<sup>a,1</sup>, Jang Mee Lee<sup>a,1</sup>, Se-Jun Kim<sup>b</sup>, Hyejin Kim<sup>c</sup>, Xiaoyan Jin<sup>a</sup>, Kang Kyun Wang<sup>d</sup>, Minho Kim<sup>b</sup>, Jeong Wook Hwang<sup>d</sup>, Wonyong Choi<sup>c</sup>, Yong-Rok Kim<sup>d,\*</sup>, Hyungjun Kim<sup>b,\*</sup>, Seong-Ju Hwang<sup>a,\*</sup>

<sup>a</sup> Center for Hybrid Interfacial Chemical Structure (CICS), Department of Chemistry and Nanoscience, Ewha Womans University, Seoul, 03760, Republic of Korea

<sup>b</sup> Department of Chemistry, Korea Advanced Institute of Science and Technology (KAIST), Daejeon, 34141, Republic of Korea

<sup>c</sup> Department of Environment Engineering, Pohang Institute of Science and Technology, Pohang, 37673, Republic of Korea

<sup>d</sup> Department of Chemistry, College of Science, Yonsei University, Seoul, 03722, Republic of Korea

### ARTICLE INFO

#### Keywords:

Hybridization  
Conductive nanosheet  
Visible light-active photocatalysts  
Interfacial electronic coupling  
Hydrophilic surface nature

### ABSTRACT

Hybridization with conductive 2D nanosheets (NSs) attracts plenty of research activities because of its effectiveness for improving the photocatalyst performance of diverse semiconductors. Here, versatile roles of conductive NSs in hybrid-type photocatalysts are systematically investigated with three representative conductive 2D NSs to synthesize highly efficient visible light-active photocatalysts. Among several conductive NS-based nanohybrids, the RuO<sub>2</sub> NS-based nanohybrid exhibits the highest photocatalytic activities. Based on systematic spectroscopic analyses, polar RuO<sub>2</sub> NS appears to be more effective as electron reservoir, photosensitizer, cocatalyst and charge carrier pathway in hybrid-type photocatalyst than MoS<sub>2</sub> and graphene NSs. The high efficiency of RuO<sub>2</sub> NS as hybridization matrix is attributable to the high surface hydrophilicity, high surface bond polarity, and enhanced interfacial electronic coupling of this hydrophilic NS with semiconductor. The present study underscores that hydrophilic conductive metal oxide NS can act as the most efficient hybridization matrix for exploring high-performance photocatalysts with strong interfacial electronic coupling.

### 1. Introduction

A great deal of research efforts has been devoted for the efficient harnessing of solar energy because of its remarkable advantage as one of the most promising sustainable energy sources [1,2]. As an efficient methodology to convert solar energy into user-friendly chemical or electrical energy [3,4], semiconductor-assisted photocatalysis boasts versatile applicabilities for the photosplitting of water to produce H<sub>2</sub> and O<sub>2</sub>, artificial photosynthesis to convert CO<sub>2</sub> into C1 compounds, and the photodegradation of harmful organic and inorganic species [5–10]. Various research strategies such as chemical substitution, the control of crystal facet, and the introduction of crystal defects have been developed to explore high-performance photocatalysts [11–13]. Among them, the hybridization with conductive 2D nanosheet (NS) like reduced graphene oxide (rGO), transition metal dichalcogenide (TMD), and transition metal oxide (TMO) is one of the most effective ways to improve the photocatalytic activity of semiconductor [5,14–19], because ultrathin thickness and wide 2D lateral dimension of exfoliated

NSs make it possible to optimize the optical and electronic properties of hybridized semiconductor [20–22]. Since the photocatalytic efficiency of semiconductor is strongly dependent on the lifetime of photoexcited electrons and holes, light absorption region, reaction kinetics of photocatalysis, and transport of photoexcited charge carriers [23–27], the beneficial effect of hybridization with 2D NSs heavily relies on their roles as electron reservoirs, photosensitizers, cocatalysts, and charge transport pathways [28–31]. Depending on the chemical composition, these inorganic NSs possess variable band structures, optical properties, and electrical conductivities, which are closely related to their capabilities for photosensitization, charge separation, and charge transport [32]. Also, tailorabile surface natures of these 2D materials can provide valuable opportunity to finely control an interfacial electronic coupling between hybridized species and to study its influence on the photocatalyst performance of the resulting nanohybrid [5,33]. Among many exfoliated NSs ever-studied, the exfoliated 2D NSs of rGO, MoS<sub>2</sub>, and RuO<sub>2</sub> are the most investigated representatives for carbon-based, TMD, and TMO NSs with high hydrophobicity, intermediate hydrophobicity/

\* Corresponding authors.

E-mail addresses: [ykim@yonsei.ac.kr](mailto:ykim@yonsei.ac.kr) (Y.-R. Kim), [linus16@kaist.ac.kr](mailto:linus16@kaist.ac.kr) (H. Kim), [hwangsju@ewha.ac.kr](mailto:hwangsju@ewha.ac.kr) (S.-J. Hwang).

<sup>1</sup> These authors contributed equally to this work.

hydrophilicity, and high hydrophilicity, respectively [5,7,8,16,28–31]. A comparative study about the hybridization effect of these NSs would be quite valuable not only in understanding mechanism responsible for the enhancement of photocatalyst performance upon hybridization but also in exploring novel high-performance NS-based hybrid photocatalyst. Despite many studies about the synthesis of conductive NS-based hybrid photocatalysts [14,34,35], we are unaware of any other systematic comparative investigation about the relative efficacies of various conductive NSs in optimizing the photocatalyst performance of semiconductor and their underlying mechanism.

In this work, a series of conductive NS ( $\text{RuO}_2$ ,  $\text{MoS}_2$ , and rGO)-based nanohybrids are synthesized not only to explore efficient visible light-active photocatalysts but also to elucidate crucial factor governing the photocatalyst functionality of hybrid-type material. The versatile roles of TMO, TMD, and rGO NSs as electron reservoirs, photosensitizers, cocatalysts, and charge transport pathways are systematically investigated with a series of well-designed experiments. To understand the effect of the chemical bonding nature of NS on the functionality of nanohybrids, the interfacial electronic couplings in the present nanohybrids are also studied with diverse spectroscopies and density functional theory (DFT) calculations.

## 2. Experimental

### 2.1. Sample preparation

The positively-charged CdS quantum dot (QD) was prepared by reacting cadmium acetate dehydrate (1.33 g, 5 mmol), 2-aminoethanethiol hydrochloride (1.42 g, 12.5 mmol), and thioacetamide (0.47 g, 6.25 mmol) in distilled water (250 mL) [36]. According to the previous report [37], the exfoliated  $\text{RuO}_2$  NS was obtained by the reaction of protonated  $\text{Na}_{0.2}\text{RuO}_2$  material with excess tetrabutylammonium ( $\text{TBA}^+$ ) ions for > 10 days. The exfoliation of  $\text{MoS}_2$  was achieved by the reaction of Li-intercalated  $\text{MoS}_2$  with distilled water, yielding metallic 1 T  $\text{MoS}_2$  NS [38]. The colloidal suspension of rGO NS was prepared by the reduction of graphene oxide synthesized by the modified Hummers' method or purchased from Aldrich Chemical (Both the rGO NSs gave similar results for the resulting nanohybrids) [5,39]. All the obtained  $\text{RuO}_2$ ,  $\text{MoS}_2$ , and rGO NSs showed negative zeta potentials of -42, -40, and -37 mV, respectively, indicating the common negative surface charges of these NSs, see Fig. S1 of Supporting information. Based on this result, intimately-coupled nanohybrids of CdS– $\text{RuO}_2$ , CdS– $\text{MoS}_2$ , and CdS–rGO were synthesized by an electrostatically-derived self-assembly between anionic NSs and cationic CdS QD, as illustrated in Fig. 1A. The colloidal suspension of cationic CdS QD was added into the colloidal suspensions of these NSs (1 mol% with respect to CdS) under vigorous stirring. After the reaction at 60 °C for 3 h, the precipitated nanohybrids were collected by high-speed centrifugation, washed thoroughly with distilled water and ethanol, and then vacuum

oven-dried at 40 °C. These materials are denoted as CdSR, CdSM, and CdSG, respectively. Additionally, the hybridization of  $\text{TiO}_2$  nanoparticles with the exfoliated  $\text{RuO}_2$ ,  $\text{MoS}_2$ , and rGO NSs was conducted by adding colloidal suspensions of each NS into aqueous dispersion of P25  $\text{TiO}_2$  nanoparticles. After the addition, the flocculation between the reactants occurred. The resulting precipitates were restored by the above-described process.

### 2.2. Characterization

The zeta potential and dynamic light scattering (DLS) data of the present  $\text{RuO}_2/\text{MoS}_2/\text{rGO}$  NSs were measured by the Zetasizer Nano ZS (Malvern Instruments). The surface areas of the conductive NSs were evaluated with  $\text{N}_2$  adsorption–desorption isotherms at liquid nitrogen temperature using Micromeritics ASAP 2020. The crystal structures of the present nanohybrids were examined with powder X-ray diffraction (XRD) analysis (Rigaku,  $\lambda = 1.5418 \text{ \AA}$ , 25 °C). Field emission-scanning electron microscopy (FE-SEM, Jeol JSM-6700 F) and energy dispersive spectrometry (EDS)–elemental mapping analyses were carried out to probe the crystal shapes and elemental compositions of the present nanohybrids. The hybrid structures of the present materials were studied with transmission electron microscopy (TEM, Jeol JEM-2100 F, 200 kV). The chemical compositions of the present nanohybrids were examined with inductively coupled plasma (ICP) spectrometry (PerkinElmer Optima-4300 DV) and EDS analysis. The photocatalytic activities of the present nanohybrids were evaluated by employing the  $\text{H}_2$  and  $\text{O}_2$  evolutions and photocurrent measurement under visible light-illumination. For both the photocatalyst activity tests, visible light from Xe lamp (300 W, Newport) with the optical cut-off filter ( $\lambda > 420 \text{ nm}$ ) and water filter was illuminated on the present materials (50 mg). The mixed solution (100 mL) of 0.1 M sodium sulfide and 0.02 M sodium sulfite was utilized as a hole scavenger ( $\text{H}_2$  evolution). For the evolution tests of  $\text{O}_2$ , 200 mg of photocatalyst was suspended in 150 mL of 0.02 M  $\text{AgNO}_3$  solution used as an electron scavenger. The evolutions of  $\text{H}_2$  and  $\text{O}_2$  gas were quantified using gas chromatography (Shimadzu GC-2014). The photocurrent generation was also examined using a potentiostat (IVIUM) with a three-electrode cell to monitor the evolution of the photocatalyst performance of CdS QD upon the hybridization. A Pt wire and a saturated calomel electrode (SCE) electrode were employed as a counter electrode and a reference electrode, respectively. 0.1 M  $\text{Na}_2\text{SO}_4$  solution was utilized as an electrolyte. The working electrode was fabricated by an indium tin oxide (ITO) glass coated with Nafion/ethanol/nanohybrids. The effective area of working electrode was 1 cm<sup>2</sup>. The electrolyte was purged with  $\text{N}_2$  gas for 0.5 h before the measurements. The evolutions of optical property and charge recombination upon hybridization were investigated with diffuse reflectance UV–vis and photoluminescence (PL) spectroscopies, respectively. Diffuse reflectance UV–vis spectroscopic measurements were carried out with a JASCO V-760 spectrometer, in which an integrating

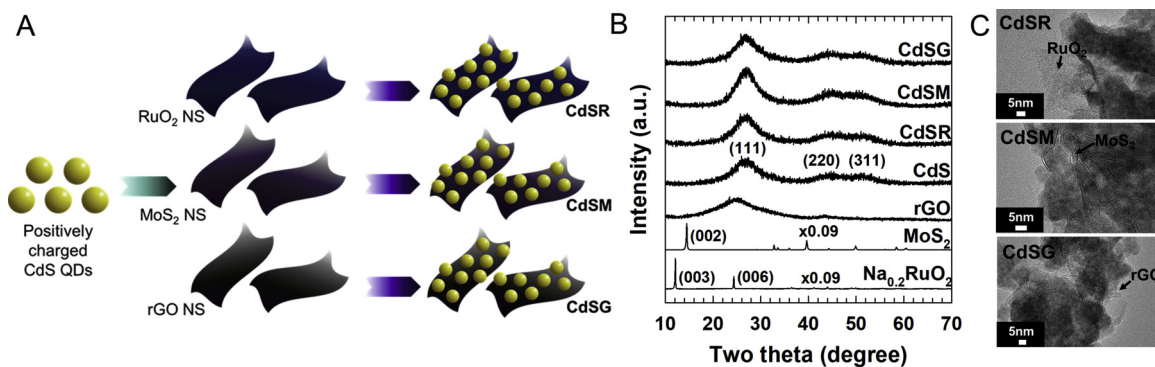


**Fig. 1.** (A) Schematic diagram of self-assembly route to CdSR, CdSM, and CdSG nanohybrids. (B) Powder XRD patterns of the pristine  $\text{Na}_{0.2}\text{RuO}_2$ ,  $\text{MoS}_2$ , rGO, CdS, CdSR, CdSM, and CdSG. (C) TEM images of CdSR, CdSM, and CdSG.

sphere and the reference  $\text{BaSO}_4$  were utilized. The PL signals from CdS-containing materials were obtained at the detection wavelength of 550 nm, which is the maximum of the PL spectra ( $\lambda_{\text{ex}} = 315 \text{ nm}$ ). To examine the interfacial electron transfer between CdS and conductive NS, time resolved photoluminescence (TRPL) spectroscopy was carried out for the present nanohybrids for assessing the PL lifetimes. The electrochemical impedance spectroscopy (EIS) measurements were carried out with an impedance analyzer (IVIUM), in which an AC voltage amplitude of 10 mV was applied in the frequency range of 100 mHz to 10 KHz. The electrical conductivities of the present NSs were measured by employing the four-point contact method for the freestanding films composed of layer-by-layer-stacked NSs prepared by the vacuum filtration of the corresponding suspensions. The X-ray photoelectron spectroscopy (XPS) data were collected for a thin layer of the sample on highly conductive copper foil using XPS spectrometer. All the XPS data were calibrated on the basis of the adventitious C 1s peak at 284.6 eV to rule out the spectral modification by the charging effect. All the present X-ray absorption spectra were measured in a transmission mode at the beam line 10C of Pohang Accelerator Laboratory (PAL, Pohang, Korea). The energies of the measured data were calibrated with a reference to simultaneously measured Cd metal spectrum. All the data were analyzed using the standard procedure as reported previously [40]. The contact angle measurements were carried for water droplet on the freestanding films of the present NSs with a DSA 100 (KRÜSS) instrument.

### 2.3. DFT calculations

DFT calculations were performed using the Vienna Ab-initio Simulation Package (VASP) [41]. We used Perdew–Burke–Ernzerhof (PBE) functional [42] to describe the exchange-correlation energy along with the DFT-D3 scheme to correct the van der Waals interaction [43,44]. We first optimized the bulk wurtzite structures of wurtzite CdS, and then constructed a non-polar (100) surface model of CdS. To build interface models of **CdSG**, **CdSM**, and **CdSR**, we interfaced  $(1 \times 1)$  CdS with  $(1 \times 3)$  graphene (**CdSG**),  $(4 \times 1)$  CdS with  $(3 \times 2)$  MoS<sub>2</sub> (**CdSM**), and  $(2 \times 2)$  CdS with  $(3 \times 3)$  RuO<sub>2</sub> (**CdSR**). Reciprocal space sampling was conducted using Monkhorst-Pack scheme with the grid dimensions of  $(7 \times 4 \times 1)$ ,  $(2 \times 5 \times 1)$ , and  $(4 \times 2 \times 1)$  for **CdSG**, **CdSM**, and **CdSR** models. Atomic structures of interface models were fully optimized with setting the cutoff energy as 400 eV, and a dipole correction was applied to eliminate an artificial interaction between periodic images along the z-direction.

## 3. Results and discussion

### 3.1. Characterization of the exfoliated RuO<sub>2</sub>, MoS<sub>2</sub>, and rGO NSs and their hybridized derivatives

As shown in Figs. S2A–C of Supporting information, the lateral sizes of these conductive NSs are determined to be  $\sim 300 \text{ nm}$  for RuO<sub>2</sub> NS,  $\sim 130 \text{ nm}$  for MoS<sub>2</sub> NS, and  $\sim 730 \text{ nm}$  for rGO NS based on the DLS analysis. According to N<sub>2</sub> adsorption–desorption isotherm analysis, the restacked NSs possess surface areas of  $\sim 12 \text{ m}^2 \text{ g}^{-1}$  for RuO<sub>2</sub> NS,  $\sim 8 \text{ m}^2 \text{ g}^{-1}$  for MoS<sub>2</sub> NS, and  $\sim 49 \text{ m}^2 \text{ g}^{-1}$  for rGO NS (Fig. S2D of Supporting information). The difference in the surface area of the present NSs can be ascribed to their dissimilar lateral sizes since the agglomeration of small-sized NSs leads to the creation of small pores unavailable for N<sub>2</sub> adsorption. As plotted in the powder XRD patterns of Fig. S2E of Supporting information, the present NSs exhibit  $(00l)$  Bragg reflections at low angle region, which are typical of these layered materials [45–47]. The d-spacings of these materials are calculated as 0.71 nm for RuO<sub>2</sub> NS, 0.63 nm for MoS<sub>2</sub> NS, and 0.37 nm for rGO NS, which are consistent with the theoretical thicknesses of these materials (0.65 nm for RuO<sub>2</sub> NS, 0.60 nm for MoS<sub>2</sub> NS, and 0.35 nm for graphene NS) [45–47].

As presented in the powder XRD patterns of Fig. 1B, all the present **CdSR**, **CdSM**, and **CdSG** nanohybrids as well as the precursor CdS QD commonly exhibit broad Bragg reflections of hexagonal CdS phase (JCPDS no. 41-1049) at  $2\theta = \sim 27^\circ$ ,  $\sim 44^\circ$ , and  $\sim 53^\circ$ , clearly demonstrating the stabilization of CdS QD in these materials. In contrast to CdS QD, no distinct NS-related Bragg reflections are discernible for all the present nanohybrids. No observation of RuO<sub>2</sub>/MoS<sub>2</sub>/rGO NSs-related peaks reflects the uniform dispersion of these NSs in the present nanohybrids, because the phase segregation of stacked NSs makes the related XRD peaks discernible [5]. As illustrated in the FE-SEM images of Fig. S3 of Supporting information, all the present **CdSR**, **CdSM**, and **CdSG** nanohybrids display the nanoscale mixing of spherical CdS QDs with highly anisotropic 2D RuO<sub>2</sub>/MoS<sub>2</sub>/rGO NSs, confirming the intimate hybridization between CdS and these NSs. The homogeneous hybridization between CdS QDs and RuO<sub>2</sub>/MoS<sub>2</sub>/rGO NSs is further evidenced by the EDS–elemental mapping analysis showing uniform distribution of all the component elements over the entire part of the nanohybrids, see Fig. S3 of Supporting information. As presented in Fig. 1C, TEM analysis for **CdSR**, **CdSM**, and **CdSG** nanohybrids provides strong evidence for intimate hybridization between CdS QDs and exfoliated RuO<sub>2</sub>/MoS<sub>2</sub>/rGO NSs. Based on the combined analysis of ICP and EDS, the molar ratios of conductive NSs in the **CdSR**, **CdSM**, and **CdSG** nanohybrids are evaluated as 0.83, 0.92, and 1.01 mol%, respectively, which are comparable to the initial ratio of 1 mol% in the precursors.

### 3.2. Photocatalytic activity tests

The effect of hybridization with exfoliated RuO<sub>2</sub>, MoS<sub>2</sub>, and rGO NSs on the photocatalytic activity of CdS QD is studied by monitoring a series of photocatalytic tests including visible light-induced H<sub>2</sub> evolution, photocurrent generation, Cr(VI) reduction by the present nano-hybrids. As can be clearly seen from Fig. 2A, all the present nanohybrids induce efficient photocatalytic H<sub>2</sub> evolution under visible light-illumination ( $\lambda > 420 \text{ nm}$ ) than does the precursor CdS QD; the rate of H<sub>2</sub> evolution is estimated as 990, 695, 486, and 471  $\mu\text{mol h}^{-1} \text{ g}^{-1}$  for **CdSR**, **CdSM**, **CdSG**, and CdS QD, respectively. Among the materials under investigation, the **CdSR** nanohybrid displays much higher visible light photocatalytic activity than does the pristine CdS QD, underscoring its excellent electrocatalyst performance. Actually, the present RuO<sub>2</sub>-based nanohybrid is one of the most promising photocatalysts for visible light-induced H<sub>2</sub> generation. The beneficial effect of hybridization with the conductive NSs on the photocatalyst performance of CdS becomes more prominent in the order of **CdSG** < **CdSM** < **CdSR**, clearly demonstrating an efficient role of RuO<sub>2</sub> NS as an additive in enhancing the photocatalyst performance of CdS QDs. Similarly, the **CdSR** nanohybrid displays a higher activity for the photocurrent generations and Cr(VI) reductions under visible light-illumination ( $\lambda > 420 \text{ nm}$ ) than do the **CdSM** and **CdSG** nano-hybrids, see Fig. 2B and C. This result confirms a better efficiency of hybridization with RuO<sub>2</sub> NS in optimizing photocatalyst functionality than those with MoS<sub>2</sub> and rGO NSs. Of noteworthy is that, in contrast to the H<sub>2</sub> evolution, the **CdSG** nanohybrid shows higher photocatalytic activity of photocurrent generation compared with that of **CdSM**, which is attributable to the higher electrical conductivity of rGO NS than MoS<sub>2</sub> NS. The beneficial effect of hybridization with conductive NSs on the photocatalyst performance is supposed to rely on the roles of these NSs as (1) electron reservoirs, (2) light sensitizers, (3) cocatalysts, and (4) charge transport pathways, respectively [28–31]. It is therefore highly demanded to systematically investigate these roles of RuO<sub>2</sub>, MoS<sub>2</sub>, and rGO NSs in the present CdS-containing nano-hybrids for understanding the mechanism responsible for the high efficacy of inorganic NS as hybridization matrix, as illustrated in Fig. 2D.

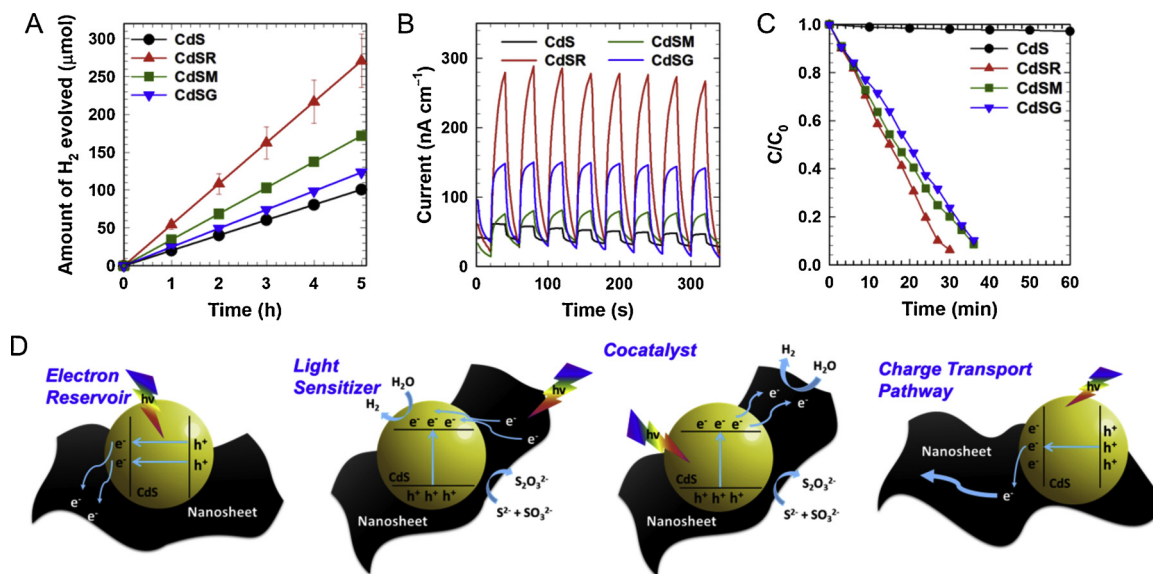


**Fig. 2.** (A) Visible light-induced H<sub>2</sub> evolution, (B) photocurrent generation, and (C) Cr(VI) reduction by CdS QD, CdSR, CdSM, and CdSG. (D) The schematic diagrams of the roles of NSS as electron reservoir, light sensitizer, cocatalyst, and charge transport pathway.

### 3.3. Relative efficacies of RuO<sub>2</sub>, MoS<sub>2</sub>, and rGO NSs as electron reservoirs

Since PL intensity is proportional to the recombination rate of photoexcited electrons and holes [48], the effect of hybridization with conductive NS on the charge recombination rate is investigated by measuring the PL spectra of the CdSR, CdSM, and CdSG nanohybrids as well as the precursor CdS QD. As plotted in Fig. 3A, the hybridization with exfoliated RuO<sub>2</sub>, MoS<sub>2</sub>, and rGO NSs commonly gives rise to the remarkable PL depression of CdS QD, indicating the effective prevention of the electron–hole recombination. This result can be regarded as strong evidence for the efficient electron transfer from CdS to conductive NS, resulting in the depression of the recombination of photoexcited electrons and holes via their spatial separation. Of prime importance is that the PL depression upon the hybridization becomes greater in the order of CdSG < CdSM < CdSR, indicating the occurrence of the most efficient interfacial electron transfer from CdS QD to RuO<sub>2</sub> NS. Additionally, the detailed mechanism of electron–hole recombination in the present nanohybrids is also investigated with TRPL spectroscopy to assess the PL lifetimes, see Fig. 3B. According to the previous report [49], all the measured PL decay signals are fitted to the biexponential function as follows:

$$I(t) = A_1 \exp(-t/\tau_1) + A_2 \exp(-t/\tau_2)$$

where the PL intensity is  $I(t)$  at a delay time of  $t$ ,  $A_1$  and  $A_2$  are the relative weights of the decay components, and  $\tau_1$  and  $\tau_2$  represent the lifetimes of two decay pathways. As summarized in Table 1, one of the exponential components shows a faster decay in the range of 0.44–0.48 ns ( $\tau_1$ ) than the decay of the other component in the range of 2.10–3.47 ns ( $\tau_2$ ). The fast component ( $\tau_1$ ) is assigned as the band edge emission responsible for the recombination of the delocalized carriers in the internal states of the CdS QD whereas the slow component ( $\tau_2$ ) would originate from the recombination of the localized carriers at the surface of CdS QD [50]. As shown in Table 1, both the PL lifetimes of CdS QD corresponding to the band edge emission and trap state emission are linearly decreased by hybridization with conductive NS in the order of CdSG > CdSM > CdSR. The fitting result is interpreted as a result of the efficient electron transfer from CdS QD to hybridized NS in the increasing order of rGO NS < MoS<sub>2</sub> NS < RuO<sub>2</sub> NS, which is in good agreement with the trends in PL intensity change (Fig. 3A). The observed relative efficiencies of conductive NSs as electron reservoirs are well consistent with the order of the photocatalyst

performances of the present nanohybrids for visible light-induced H<sub>2</sub> evolution reaction. The efficient role of conductive NSs as electron reservoirs is further evidenced by a comparative study of photocatalytic Cr(VI) reduction by the CdSR, CdSM, and CdSG nanohybrids with and without RhB reagent, since RhB molecule can act as photosensitizer to inject photoexcited electron into semiconductor [51]. As plotted in Fig. S4 of Supporting information, the addition of RhB reagent leads to the remarkable enhancement of the photoreduction of Cr(VI) by the CdSR, CdSM, and CdSG nanohybrids, indicating the occurrence of an effective electron injection from RhB into these nanohybrids. Among the present nanohybrids, CdSR nanohybrid displays the most prominent enhancement upon the incorporation of RhB molecule, highlighting the most efficient interfacial electron transfer from RhB to CdSR. This result can be regarded as another evidence for the efficient role of RuO<sub>2</sub> NS as electron reservoir. The present experiments clearly demonstrate a significant contribution of the role of conductive NS as electron reservoir to the improvement of photocatalytic activity upon the hybridization with conductive NS.

### 3.4. Relative efficacies of RuO<sub>2</sub>, MoS<sub>2</sub>, and rGO NSs as photosensitizers

The efficiencies of these conductive NSs as photosensitizers are examined by measuring the optical properties of CdSR, CdSM, and CdSG as well as the precursor CdS QD, RuO<sub>2</sub> NS, MoS<sub>2</sub> NS, and rGO NS. As depicted in the diffuse reflectance UV-vis spectra of Fig. 4A, the CdS QD shows a distinct absorption edge corresponding to its bandgap energy whereas no absorption edge is discernible for both the rGO and RuO<sub>2</sub> NSs, reflecting their metallic properties. The MoS<sub>2</sub> NS exhibits weaker visible light absorptivity than do the rGO and RuO<sub>2</sub> NSs, strongly suggesting a lower electrical conductivity of MoS<sub>2</sub> [17]. In comparison with the CdS QD, all the present CdSR, CdSM, and CdSG nanohybrids demonstrate much stronger absorption of visible light, indicating the enhancement of visible light absorption caused by the hybridized conductive NS. The visible light absorptivity of the present nanohybrids becomes higher in the order of CdSG < CdSM < CdSR, indicating the highest efficacy of RuO<sub>2</sub> NS as photosensitizer. Of noteworthy is that, despite lower absorptivity of MoS<sub>2</sub> than rGO, CdSM shows stronger visible light absorption than does CdSG, strongly suggesting more efficient electronic coupling of CdS with MoS<sub>2</sub> than with rGO. In addition to the enhancement of visible light absorption, the hybridization with the conductive NSs causes a distinct red-shift of the absorption edge of CdS, indicating the expansion of light absorption

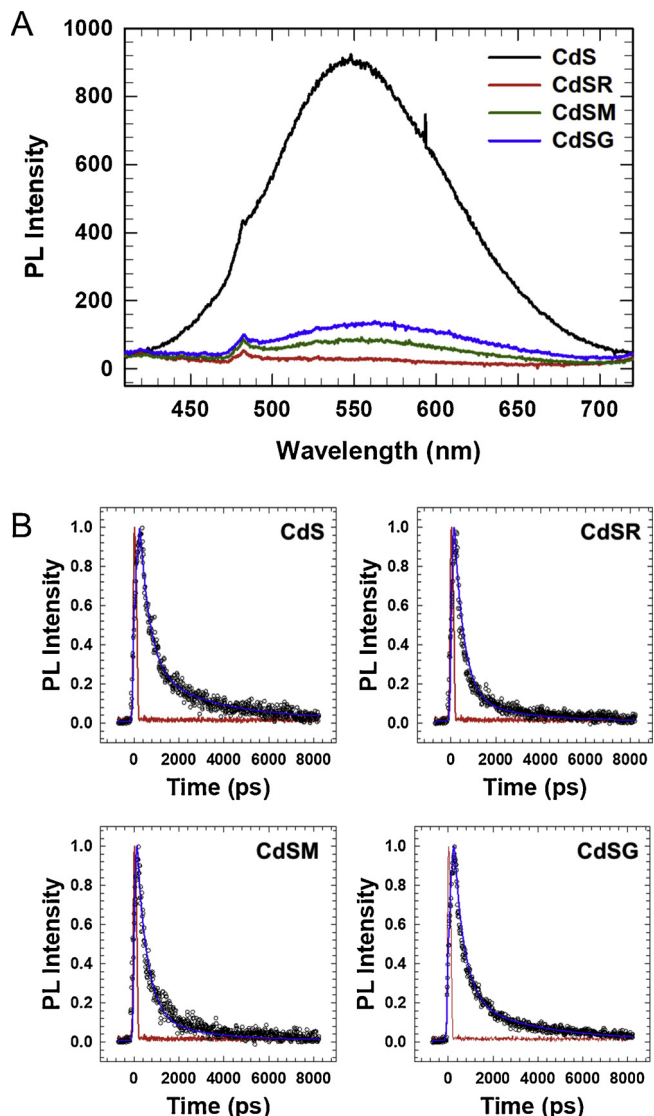


**Fig. 3.** (A) PL spectra and (B) TRPL decays of CdS QD, CdSR, CdSM, and CdSG. In (B), the blue lines and red lines represent the fitted lines from the fitting analysis and the instrumental response functions, respectively (For interpretation of the references to colour in this figure legend, the reader is referred to the web version of this article).

**Table 1**  
PL decay parameters of the precursor CdS QD and the CdSG, CdSM, and CdSR nanohybrids.

Sample	$\tau_1$ (ns)	A <sub>1</sub> (%)	$\tau_2$ (ns)	A <sub>2</sub> (%)	$\chi^2$
CdS QD	0.475	81.3	3.47	18.7	0.996
CdSG	0.465	83.5	3.15	16.5	1.016
CdSM	0.443	88.8	2.41	11.2	0.989
CdSR	0.441	89.9	2.10	10.1	1.015

region. According to the determination of the bandgap energy ( $E_g$ ) via the linear interpolation of  $\alpha/S$  absorption coefficients, the  $E_g$  values of the present materials are estimated to be ~2.80 eV for precursor CdS QD, ~2.32 eV for CdSR, ~2.40 eV for CdSM, and ~2.67 eV for CdSG, respectively. The alteration of  $E_g$  upon hybridization increases in the order of CdSG < CdSM < CdSR. Since negligible structural modification of CdS QD upon the hybridization with 2D inorganic NSs strongly suggests no significant alteration of its band structure, the observed decrease of  $E_g$  after hybridization can be ascribed to the occurrence of an interfacial

electron excitation from valence band of CdS QDs to empty band of 2D inorganic NSs, resulting in the decrease of absorption energy. Such a direct electronic transition between hybridized nanospecies with significant lowering of  $E_g$  has been reported for exfoliated 2D nanosheet-based hybrid materials with unusually strong interfacial electronic coupling [52,53]. This interpretation is evidenced by the stronger redshift of absorption edge for CdSR with stronger electronic coupling than for CdSM and CdSG nanohybrids with weaker electronic coupling [53,54]. The present UV-vis results clearly demonstrate that the polar RuO<sub>2</sub> and MoS<sub>2</sub> NSs can act as highly effective photosensitizers, which is superior to rGO NS. The wavelength-dependent H<sub>2</sub> generation is also examined for the present nanohybrids using several cutoff filters. As can be seen clearly from Fig. 4B, both the CdSR and CdSM nanohybrids can induce more efficient H<sub>2</sub> generation upto 450 nm than the other materials, confirming the effective roles of RuO<sub>2</sub> and MoS<sub>2</sub> NSs as photosensitizers.

To further verify the relative efficiencies of the exfoliated RuO<sub>2</sub>, MoS<sub>2</sub>, and rGO NSs as visible light sensitizers, these NSs are hybridized with wide bandgap semiconductor of TiO<sub>2</sub>, i.e. P25. The resulting TiO<sub>2</sub>-RuO<sub>2</sub>, TiO<sub>2</sub>-MoS<sub>2</sub>, and TiO<sub>2</sub>-rGO nanohybrids are tested as photocatalysts for visible light-induced H<sub>2</sub> generation ( $\lambda > 420$  nm) to evaluate their roles as visible light photosensitizers. As plotted in Fig. 4C, the TiO<sub>2</sub>-RuO<sub>2</sub> nanohybrid displays a distinct photocatalytic activity for visible light-induced production of H<sub>2</sub> gas, which is in stark contrast to the weak photocatalytic activities of TiO<sub>2</sub>-MoS<sub>2</sub> and TiO<sub>2</sub>-rGO nanohybrids. All the present experimental findings highlight that the exfoliated RuO<sub>2</sub> NS can be used as the most efficient photosensitizer for exploring visible light photocatalysts.

### 3.5. Relative efficacies of RuO<sub>2</sub>, MoS<sub>2</sub>, and rGO NSs as cocatalysts

To probe the relative efficacies of the exfoliated RuO<sub>2</sub>, MoS<sub>2</sub>, and rGO NSs as cocatalysts, the CdS QD is electrophoretically deposited on transparent ITO substrate and then the top surface of the resulting films is tightly covered with these NSs using spin coating technique, as illustrated in Fig. 4D. The full coverage of multilayer film surface by the RuO<sub>2</sub>, MoS<sub>2</sub>, and rGO NSs is confirmed by FE-SEM analysis. Since the photocatalytic H<sub>2</sub> generation occurs only on the top NS layer acting as the photocatalysis reaction sites, the photocatalyst performances of these films provide a quantitative measure for the cocatalyst roles of RuO<sub>2</sub>, MoS<sub>2</sub>, and rGO NSs for providing photocatalyst reaction sites. To avoid the interference effect of light absorption by top conductive NS layer on the photocatalytic activities of the resulting films, H<sub>2</sub> generation experiments are carried out with the illumination of visible light from the back side of film (Fig. 4D). As plotted in Fig. 4E, the RuO<sub>2</sub> NS-covered film shows a significantly higher photocatalytic activity for visible light-induced H<sub>2</sub> generation than does uncovered CdS film, clearly demonstrating the certain role of this metal oxide NS as a cocatalyst. Conversely, the other NS-covered films exhibit only a weak improvement of photocatalytic activity compared with the bare CdS film. The present result clearly demonstrates the superior role of RuO<sub>2</sub> NS as a cocatalyst over the other NSs.

### 3.6. Relative efficacies of RuO<sub>2</sub>, MoS<sub>2</sub>, and rGO NSs as charge transport pathways

The evolution of electron transport property upon hybridization with conductive NS is crucial in optimizing the migration of photo-excited electrons and holes into the surface reaction sites [55]. The relative efficacies of exfoliated RuO<sub>2</sub>, MoS<sub>2</sub>, and rGO NSs as charge transport pathways are investigated by measuring the EIS data of the CdSR, CdSM, and CdSG nanohybrids and the electrical conductivities of the hybridized NSs. As depicted in the EIS data of Fig. 5A, the charge transfer (CT) properties of the present materials become improved by hybridization with conductive NS in the order of MoS<sub>2</sub> NS < rGO NS < RuO<sub>2</sub> NS, emphasizing the superior role of RuO<sub>2</sub> NS over rGO

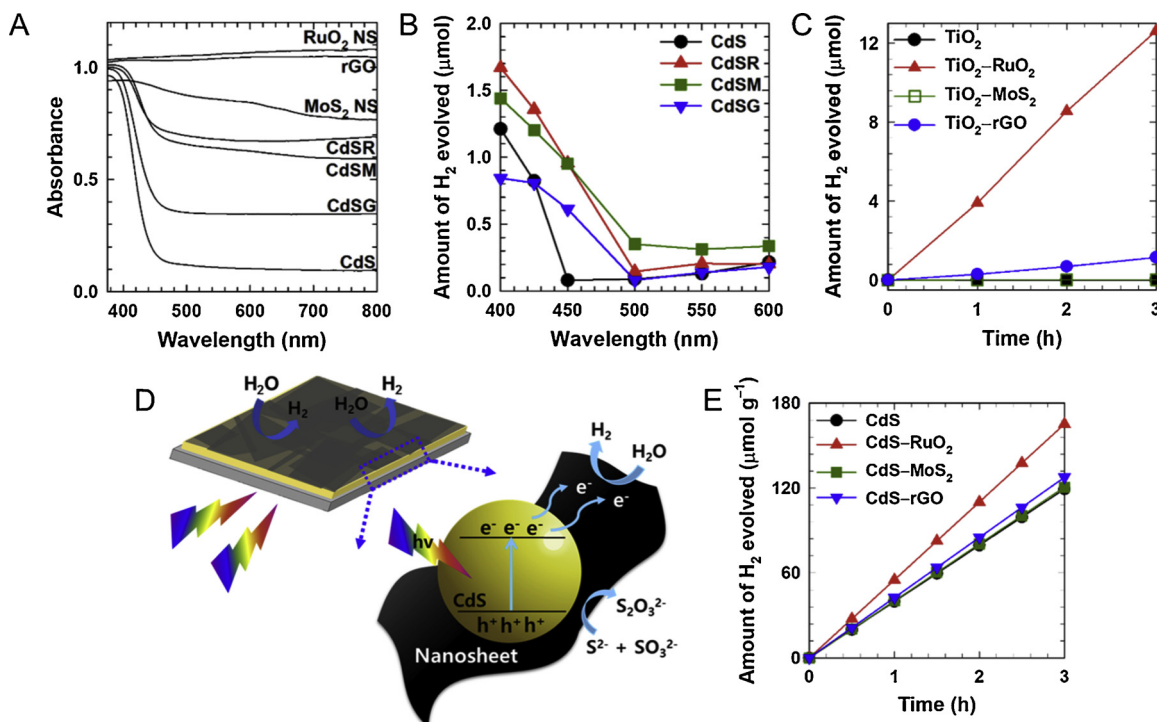


**Fig. 4.** (A) Diffuse reflectance UV – vis spectra of CdS QD, RuO<sub>2</sub> NS, MoS<sub>2</sub> NS, rGO NS, CdSR, CdSM, and CdSG. (B) Wavelength dependence of H<sub>2</sub> evolution by CdS QD, CdSR, CdSM, and CdSG. (C) Visible light-induced H<sub>2</sub> evolution by TiO<sub>2</sub>, TiO<sub>2</sub>–RuO<sub>2</sub> nanohybrid, TiO<sub>2</sub>–MoS<sub>2</sub> nanohybrid, and TiO<sub>2</sub>–rGO nanohybrid. (D) Schematic diagram for the experimental setup for probing the relative efficiency of NS as a cocatalyst. (E) Visible light-induced H<sub>2</sub> evolution by CdS films covered with RuO<sub>2</sub>, MoS<sub>2</sub>, and rGO NSs.

and MoS<sub>2</sub> NSs as CT pathway. This result is further confirmed by the electrical conductivity measurement for freestanding films composed of corresponding layer-by-layer-stacked exfoliated NSs [56–58]. As plotted in Fig. 5B, the electrical resistances of these NS films become smaller in the order of MoS<sub>2</sub> NS < rGO NS < RuO<sub>2</sub> NS, which is in good agreement with the EIS data. These results underscore that the efficiency of the present conductive NSs as electron pathways increases in the order of MoS<sub>2</sub> NS < rGO NS < RuO<sub>2</sub> NS. Considering the better photocatalyst performance of CdSM than CdSG for H<sub>2</sub> generation, the role of charge transport pathway seems to make only a limited contribution to the enhanced photocatalytic activities of the present nanohybrids (Fig. 2A). However, a better performance of CdSG than CdSM for photocurrent generation underscores the importance of high conductivity for creating photocurrent.

### 3.7. Interfacial electronic coupling of CdS with RuO<sub>2</sub>, MoS<sub>2</sub>, and rGO NSs

Since the electronic coupling between CdS and incorporated NSs would have remarkable influence on the roles of these NSs as electron reservoirs, photosensitizers, and charge transport pathway, the interfacial CT between CdS QDs and exfoliated RuO<sub>2</sub>/MoS<sub>2</sub>/rGO NSs is investigated with surface-sensitive XPS technique. The Cd 3d XPS data of the present CdSR, CdSM, and CdSG nanohybrids as well as CdS QD are presented in Fig. 6A. Typical spectral features of CdS phase are commonly observed for all the present nanohybrids [59]. The hybridization with RuO<sub>2</sub> NSs leads to the significant displacement of the Cd 3d<sub>5/2</sub> and Cd 3d<sub>3/2</sub> peaks of CdS component toward high energy side, indicating an electron transfer from CdS to RuO<sub>2</sub>. This finding provides strong evidence for the role of RuO<sub>2</sub> as an efficient electron reservoir. In comparison with the CdSR nanohybrid, weaker spectral modifications of Cd 3d XPS features occur for the CdSM and CdSG nanohybrids, highlighting weaker interfacial electron coupling with MoS<sub>2</sub> and rGO

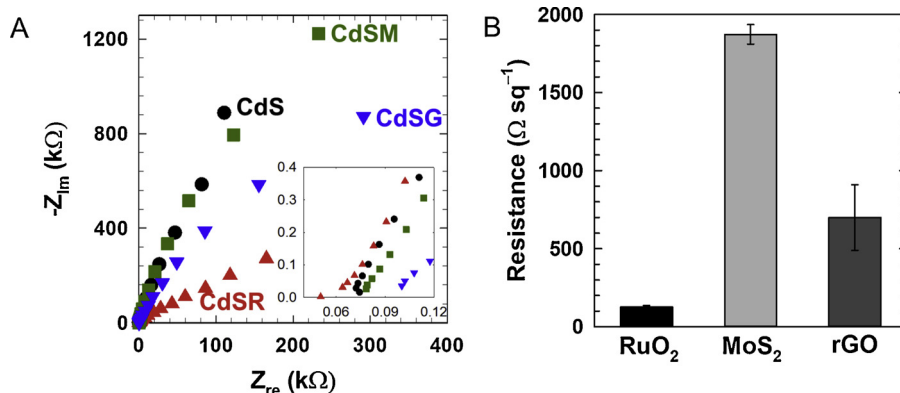


**Fig. 5.** (A) EIS data of CdS QD, CdSR, CdSM, and CdSG. The inset shows the close-up view at low impedance range. (B) Electrical resistances of the freestanding films of restacked RuO<sub>2</sub>, MoS<sub>2</sub>, and rGO NSs.

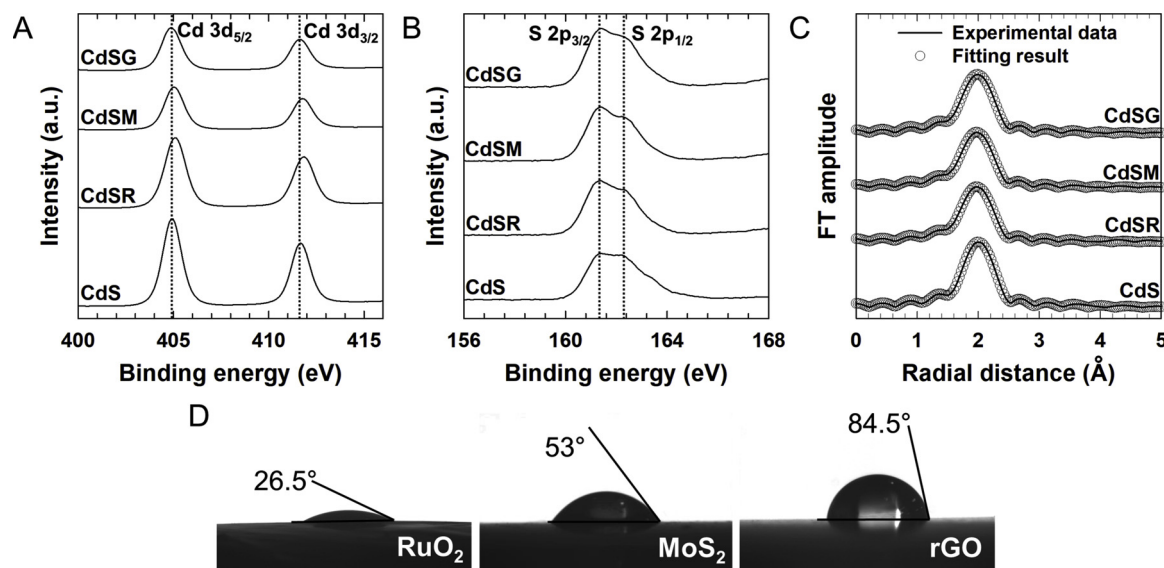


**Fig. 6.** (A) Cd 3d XPS, (B) S 2p XPS, and (C) Cd K-edge EXAFS data of CdS QD, CdSR, CdSM, and CdSG. (D) Contact angle images of water droplet on restacked RuO<sub>2</sub>, MoS<sub>2</sub>, and rGO NS films.

NSs than RuO<sub>2</sub> NS. The enhanced electronic coupling between CdS QD and RuO<sub>2</sub> NS is mainly responsible for the remarkable evolution of the PL and diffuse reflectance UV–vis spectra of CdS upon the hybridization with RuO<sub>2</sub> NS. In contrast to the Cd 3d XPS data, there is only a weak shift in the S 2p XPS spectra, indicating the negligible change of sulfur species upon the hybridization, see Fig. 6B.

The evolution of the local structure of CdS upon the hybridization with conductive NSs is investigated with Cd K-edge extended X-ray absorption fine structure (EXAFS) analysis. As presented in Fig. 6C, all the present nanohybrids display typical Fourier transformed (FT) data of CdS, indicating the maintenance of CdS lattice upon the hybridization. All the present EXAFS spectra can be well-reproduced with CdS structure. As summarized in Table S1 of Supporting information, the hybridization with conductive NSs leads to the decrease of (Cd–S) bond distance, indicating the increase of (Cd–S) bond covalency due to the electron transfer from CdS to hybridized NS. This bond shortening upon hybridization is more prominent for CdSR and CdSM than for CdSG, confirming more efficient electron transfer from CdS to polar RuO<sub>2</sub>/MoS<sub>2</sub> NSs. Summarizing the XPS and EXAFS results presented here, the interfacial CT of the present materials becomes enhanced in the order of CdSG < CdSM < CdSR.

To understand the difference in the interfacial electronic coupling between CdS and additive NSs, the surface hydrophilicities of these NSs are probed by contact angle measurement for the corresponding free-standing films. Because of unusually high anisotropic 2D structures of incorporated NSs, the surface natures of these NSs largely affect an interfacial interaction of conductive NSs with CdS QDs. As illustrated in Fig. 6D, the RuO<sub>2</sub> film exhibits a small contact angle of 26.5°, reflecting the hydrophilic surface nature of this metal oxide NSs. In comparison, larger contact angles of 53.0° and 84.5° are discernible for MoS<sub>2</sub> and rGO films, respectively. The observed order of the surface hydrophilicity of the present NSs, i.e. rGO NS < MoS<sub>2</sub> NS < RuO<sub>2</sub> NS, is in good agreement with the observed trend of electronic coupling, underscoring the crucial role of surface bonding nature in enhancing electronic coupling with polar semiconductor like CdS. The observed remarkable difference in the surface hydrophilicity of these conductive NSs causes a significant alteration of interfacial interaction at the heterojunction of the present nanohybrids.

The electronic coupling of CdS with hybridized RuO<sub>2</sub>, MoS<sub>2</sub>, and rGO NSs is theoretically investigated with DFT calculations. As shown in Fig. 7A–C, DFT-optimized structures yield interdistance of 2.52 Å, 2.85 Å, and 3.37 Å for CdS–RuO<sub>2</sub>, CdS–MoS<sub>2</sub>, and CdS–rGO

interfaces, respectively. Bader charge [60] and planar-averaged differential charge density ( $\Delta\rho$  of before and after hybridization) further elucidate that a closer interaction enables the more signified CT; the CT at the CdS–rGO interface marginally occurs ( $0.01e^-$  from CdS to rGO), while an order or magnitude enhanced CT is found for the CdS–MoS<sub>2</sub> interface ( $0.11e^-$  from CdS to MoS<sub>2</sub>), and even another order of magnitude enhanced CT is found for the CdS–RuO<sub>2</sub> interface ( $1.14e^-$  from CdS to RuO<sub>2</sub>). This trend is in consistent with our experiments.

The band structure analysis clearly demonstrates that the enhanced CT at the CdS–RuO<sub>2</sub> interface is manifested by the orbital–orbital hybridization. The valence band (VB) edges of CdS mostly consist of *p*-bands of sulfur atoms (Fig. S5 of Supporting information); *px*-band for the VB maximum and *pz*-band for the second maximum. After the hybridization of CdS with RuO<sub>2</sub>, as shown in Fig. 7D and E, the *pz*-bands are significantly hybridized with the RuO<sub>2</sub> states, which provide a channel for electron transfer. The DFT results presented here underscore that the efficiency of electronic coupling of conductive NS with hybridized semiconductor is well-correlated with its surface hydrophilicity.

### 3.8. XRD, FE-SEM, photocatalytic O<sub>2</sub> evolution, and PL analyses of Ag<sub>3</sub>PO<sub>4</sub>–RuO<sub>2</sub>/MoS<sub>2</sub>/rGO nanohybrids

The versatile usefulness of hybridization with metal oxide NS in exploring the high-performance photocatalyst is further evidenced by the comparative study for conductive NS-based nanohybrids containing oxygen-evolving Ag<sub>3</sub>PO<sub>4</sub> photocatalyst. These nanohybrids are synthesized by the crystal growth of Ag<sub>3</sub>PO<sub>4</sub> on the exfoliated rGO/MoS<sub>2</sub>/RuO<sub>2</sub> NSs, according to the previously-reported method [5]. As plotted in Fig. S6 of Supporting information, the Ag<sub>3</sub>PO<sub>4</sub>–RuO<sub>2</sub> nanohybrid shows much higher photocatalytic activity for visible light-induced O<sub>2</sub> generation than does the pristine Ag<sub>3</sub>PO<sub>4</sub>, underscoring the excellent photocatalyst performance of the RuO<sub>2</sub> NS-based nanohybrid. The photocatalyst functionality of the Ag<sub>3</sub>PO<sub>4</sub>–RuO<sub>2</sub> nanohybrid is better than those of the Ag<sub>3</sub>PO<sub>4</sub>–MoS<sub>2</sub> and Ag<sub>3</sub>PO<sub>4</sub>–rGO nanohybrids, verifying universal role of conductive metal oxide NS as a superior hybridization matrix. A strong electronic coupling of Ag<sub>3</sub>PO<sub>4</sub> with RuO<sub>2</sub> NS is confirmed by the most prominent depression of PL upon the hybridization with RuO<sub>2</sub> NS (Fig. S6 of Supporting information). The present experimental finding underscores that the hybridization with hydrophilic conductive metal oxide NS can provide a highly effective way to enhance the photocatalytic activity of semiconductors and the

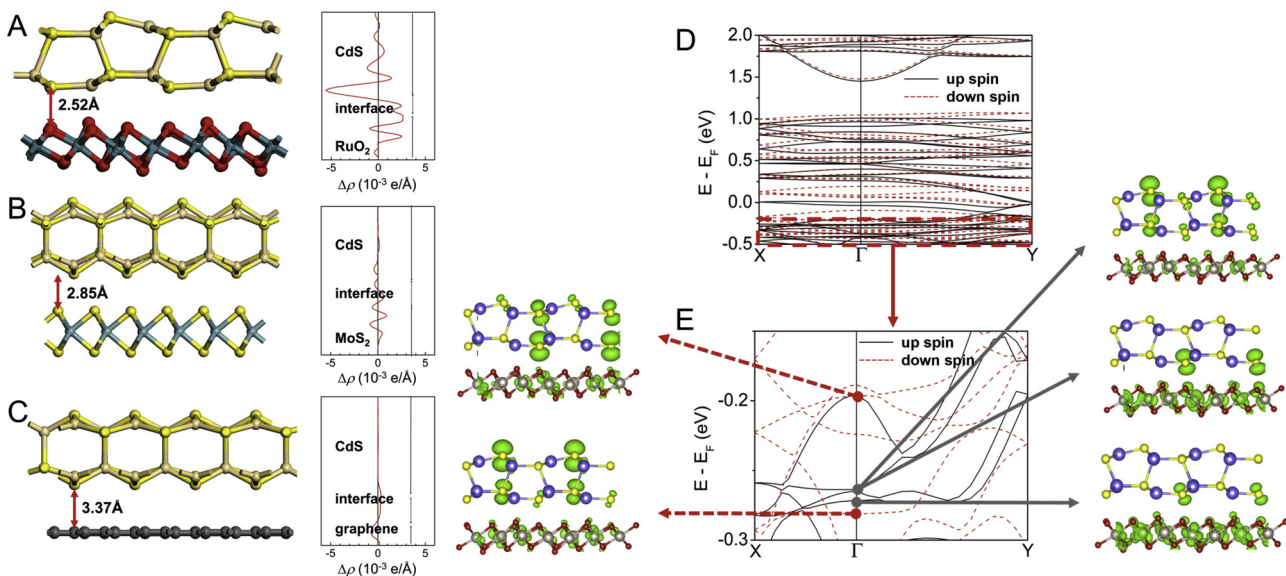


**Fig. 7.** DFT-optimized structures and plane-averaged differential charge density along normal direction to the interfaces of (A) CdS – RuO<sub>2</sub> (CdSR), (B) CdS – MoS<sub>2</sub> (CdSM), and (C) CdS – rGO (CdSG). (D) Band structure of CdS – RuO<sub>2</sub> interfacial system and (E) enlargement of valence band (VB) edges of CdS. VB states near the edge are visualized using band decomposed partial charge density (isovalue =  $0.007 \text{ \AA}^{-3}$ ), which shows a significant orbital – orbital hybridization between  $p_z$ -band of CdS and RuO<sub>2</sub> states.

roles of conductive NSs as charge reservoir/photosensitizer and charge transport pathway are crucial in enhancing the photocatalyst performance of the resulting nanohybrid for photocatalytic reaction and photocurrent generation, respectively.

#### 4. Conclusions

In conclusion, systematic comparative experiments presented here enable to evaluate the relative efficiencies of the present representative NSs for versatile roles; (1) electron reservoir efficiency: rGO NS < MoS<sub>2</sub> NS < RuO<sub>2</sub> NS, (2) photosensitizer efficiency: rGO NS < MoS<sub>2</sub> NS < RuO<sub>2</sub> NS, (3) cocatalyst efficiency: MoS<sub>2</sub> NS < rGO NS < RuO<sub>2</sub> NS, and (4) electron pathway efficiency: MoS<sub>2</sub> NS < rGO NS < RuO<sub>2</sub> NS. Among the present materials, the RuO<sub>2</sub> NS-based CdSR nanohybrid is one of the most promising photocatalysts for visible light-induced H<sub>2</sub> generation. The present study clearly demonstrates that the conductive metal oxide NS with high surface hydrophilicity can act as the most effective hybridization matrix for enhancing the photocatalytic activity of semiconductor. The improvement of photocatalyst performance upon the hybridization with the conductive NSs is concluded to heavily rely on their roles as charge reservoirs to suppress the electron – hole recombination and photosensitizers to enhance visible light harnessing. The role of conductive NS as electron transport pathway is more important for photocurrent generation than for H<sub>2</sub> generation. Based on the results of XPS, EXAFS, contact angle measurement, and DFT calculation, the excellent efficiency of conductive metal oxide NS as hybridization matrix can be understood as a result of its polar surface bonding nature, allowing a strong interfacial electronic coupling with semiconductor. We can conclude that an interfacial electronic coupling is the most crucial factor in designing and synthesizing high-performance hybrid-type photocatalysts.

Considering the fact that, in addition to photocatalyst performance, the electrocatalyst and electrode functionalities of inorganic solids can be effectively enhanced by hybridization with conductive NSs [61], comparative study with representative conductive NS-based hybrid electrocatalysts/electrodes can give useful insight for optimizing these electrochemistry-related functionalities of hybrid materials. Our current project is to employ the present conductive rGO, MoS<sub>2</sub>, and RuO<sub>2</sub> NSs as hybridization matrices for diverse electrochemically-active materials like metal, metal chalcogenide, and metal hydroxides for

elucidating crucial factors in synthesizing efficient NS-based hybrid electrocatalysts and electrodes.

#### Declarations of interest

None.

#### Acknowledgments

This work was supported by the National Research Foundation of Korea (NRF) grant funded by the Korea government (MSIP) (No. NRF-2017R1A2A17069463) and by the Korea government (MSIT) (No. NRF-2017R1A5A1015365). The experiments at PAL were supported in part by MOST and POSTECH.

#### Appendix A. Supplementary data

Supplementary material related to this article can be found, in the online version, at doi:<https://doi.org/10.1016/j.apcatb.2019.117875>.

#### References

- [1] V. Devabhaktuni, M. Alam, S.S.S.R. Depuru, R.C. Green II, D. Nims, C. Near, Solar energy: trends and enabling technologies, *Renew. Sustain. Energy Rev.* 19 (2013) 555–564.
- [2] G. Zhang, G. Liu, L. Wang, J.T.S. Irvine, Perovskite photocatalysts for solar energy utilization, *Chem. Soc. Rev.* 45 (2016) 5951–5984.
- [3] H. Takeda, K. Ohashi, A. Sekine, O. Ishitani, Photocatalytic CO<sub>2</sub> reduction using Cu (I) photosensitizers with a Fe(II) catalyst, *J. Am. Chem. Soc.* 138 (2016) 4354–4357.
- [4] J. Li, N. Wu, Semiconductor-based photocatalysts and photoelectrochemical cells for solar fuel generation: a review, *Catal. Sci. Technol.* 5 (2015) 1360–1384.
- [5] J.M. Lee, E.K. Mok, S. Lee, N.-S. Lee, L. Debbichi, H. Kim, S.-J. Hwang, A conductive hybridization matrix of RuO<sub>2</sub> two-dimensional nanosheets: a hybrid-type photocatalyst, *Angew. Chem. Int. Ed.* 55 (2016) 8546–8550.
- [6] Z. He, J. Tang, J. Shen, J. Chen, S. Song, Enhancement of photocatalytic reduction of CO<sub>2</sub> to CH<sub>4</sub> over TiO<sub>2</sub> nanosheets by modifying with sulfuric acid, *Appl. Surf. Sci.* 364 (2016) 416–427.
- [7] C. Zhu, L. Zhang, B. Jiang, J. Zheng, P. Hu, S. Li, M. Wu, W. Wu, Fabrication of Z-scheme Ag<sub>3</sub>PO<sub>4</sub>/MoS<sub>2</sub> composites with enhanced photocatalytic activity and stability for organic pollutant degradation, *Appl. Surf. Sci.* 377 (2016) 99–108.
- [8] H. Li, Y. Wang, G. Chen, Y. Sang, H. Jiang, J. He, X. Li, H. Liu, Few-layered MoS<sub>2</sub> nanosheets wrapped ultrafine TiO<sub>2</sub> nanobelts with enhanced photocatalytic property, *Nanoscale* 8 (2016) 6101–6109.
- [9] Q. Li, Y. Xia, C. Yang, K. Lv, M. Lei, Building a direct Z-scheme heterojunction photocatalyst by ZnIn<sub>2</sub>S<sub>4</sub> nanosheets and TiO<sub>2</sub> hollowspheres for highly-efficient

- artificial photosynthesis, *Chem. Eng. J.* 349 (2018) 287–296.
- [10] T. Huang, Y. Li, X. Wu, K. Lv, Q. Li, M. Li, D. Du, H. Ye, In-situ transformation of  $\text{Bi}_2\text{WO}_6$  to highly photoreactive  $\text{Bi}_2\text{WO}_6@\text{Bi}_2\text{S}_3$  nanoplate via ion exchange, *Chin. J. Catal.* 39 (2018) 718–727.
- [11] D. Prime, G. Zeng, R. Leute, M. Walter, L. Mayrhofer, M. Niederberge, Chemical substitution-alignment of the surface potentials for efficient charge transport in nanocrystalline  $\text{TiO}_2$  photocatalysts, *Chem. Mater.* 28 (2016) 4223–4230.
- [12] S. Wang, H. Chen, G. Gao, T. Butburee, M. Lyu, S. Thaweesak, J.-H. Yun, A. Du, G. Liu, L. Wang, Synergistic crystal facet engineering and structural control of  $\text{WO}_3$  films exhibiting unprecedented photoelectrochemical performance, *Nano Energy* 24 (2016) 94–102.
- [13] J. Yu, J. Low, W. Xiao, P. Zhou, M. Jaroniec, Enhanced photocatalytic  $\text{CO}_2$ -reduction activity of anatase  $\text{TiO}_2$  by coexposed {001} and {101} facets, *J. Am. Chem. Soc.* 136 (2014) 8839–8842.
- [14] Y.K. Jo, J.M. Lee, S. Son, S.-J. Hwang, 2D inorganic nanosheet-based hybrid photocatalysts: design, applications, and perspectives, *J. Photochem. Photobiol. C: Photochem. Rev.* (2019), <https://doi.org/10.1016/j.jphotchemrev.2018.03.002>.
- [15] P. Mohammadyari, A. Nezamzadeh-Ejhieh, Supporting of mixed  $\text{ZnS}$ - $\text{NiS}$  semiconductors onto clinoptilolite nano-particles to improve its activity in photo-degradation of 2-nitrotoluene, *RSC Adv.* 5 (2015) 75300–75310.
- [16] D. Lang, T. Shen, Q. Xiang, Roles of  $\text{MoS}_2$  and graphene as cocatalysts in the enhanced visible-light photocatalytic  $\text{H}_2$  production activity of multiarmed  $\text{CdS}$  nanorods, *ChemCatChem* 7 (2015) 943–951.
- [17] Y. Xia, Q. Li, K. Lv, D. Tang, M. Li, Superiority of graphene over carbon analogs for enhanced photocatalytic  $\text{H}_2$ -production activity of  $\text{ZnIn}_2\text{S}_4$ , *Appl. Catal. B: Environ.* 206 (2017) 344–352.
- [18] Y. Li, Z. Yin, G. Ji, Z. Liang, Y. Xue, Y. Guo, K. Tian, X. Wang, H. Cui, 2D/2D/2D heterojunction of  $\text{Ti}_3\text{C}_2$  MXene/ $\text{MoS}_2$  nanosheets/ $\text{TiO}_2$  nanosheets with exposed {001} facets toward enhanced photocatalytic hydrogen production activity, *Appl. Catal. B: Environ.* 246 (2019) 12–20.
- [19] H. Li, S. Xiao, J. Zhou, J. Zhao, F. Liu, G. Li, D. Zhang, A flexible  $\text{CdS}$  nanorods-carbon nanotubes/stainless steel mesh photoanode for boosted photoelectrocatalytic hydrogen evolution, *Chem. Commun.* 55 (2019) 2741–2744.
- [20] L. Zhang, J. Lian, L. Wu, Z. Duan, J. Jiang, L. Zhao, Synthesis of a thin-layer  $\text{MnO}_2$  nanosheet-coated  $\text{Fe}_3\text{O}_4$  nanocomposite as a magnetically separable photocatalyst, *Langmuir* 30 (2014) 7006–7013.
- [21] J.L. Gunjakar, I.Y. Kim, J.M. Lee, Y.K. Jo, S.-J. Hwang, Exploration of nanostructured functional materials based on hybridization of inorganic 2D nanosheets, *J. Phys. Chem. C* 118 (2014) 3847–3863.
- [22] H. Wang, L. Zhang, Z. Chen, J. Hu, S. Li, Z. Wang, J. Liu, X. Wang, Semiconductor heterojunction photocatalysts: design, construction, and photocatalytic performances, *Chem. Soc. Rev.* 43 (2014) 5234–5244.
- [23] J. Ran, J. Zhang, J. Yu, M. Jaroniec, S.Z. Qiao, Earth-abundant cocatalysts for semiconductor-based photocatalytic water splitting, *Chem. Soc. Rev.* 43 (2014) 7787–7812.
- [24] C. Han, Z. Chen, N. Zhang, J.C. Colmenares, Y.-J. Xu, Hierarchically  $\text{CdS}$  decorated 1D  $\text{ZnO}$  nanorods-2D graphene hybrids: low temperature synthesis and enhanced photocatalytic performance, *Adv. Funct. Mater.* 25 (2015) 221–229.
- [25] Y. Li, P. Hang, Y. Hou, S. Peng, X. Kuang, Oriented  $\text{Zn}_m\text{In}_2\text{S}_{m+3}@\text{In}_2\text{S}_3$  heterojunction with hierarchical structure for efficient photocatalytic hydrogen evolution, *Appl. Catal. B: Environ.* 244 (2019) 604–611.
- [26] W. Wang, X. Zhao, Y. Cao, Z. Yan, R. Zhu, Y. Tao, X. Chen, D. Zhang, G. Li, D.L. Phillips, Copper phosphide-enhanced lower charge trapping occurrence in graphitic- $\text{C}_3\text{N}_4$  for efficient noble-metal-Free photocatalytic  $\text{H}_2$  evolution, *ACS Appl. Mater. Interfaces* 11 (2019) 16527–16537.
- [27] S. Xiao, W. Dai, X. Liu, D. Pan, H. Zou, G. Li, G. Zhang, C. Su, D. Zhang, W. Chen, H. Li, Microwave-induced metal dissolution synthesis of core-shell copper nanowires/ $\text{ZnS}$  for visible light photocatalytic  $\text{H}_2$  evolution, *Adv. Energy Mater.* (2019), <https://doi.org/10.1002/aenm.201900775>.
- [28] Y. Wang, J. Yu, W. Xiao, Q. Li, Microwave-assisted hydrothermal synthesis of graphene based  $\text{Au}-\text{TiO}_2$  photocatalysts for efficient visible-light hydrogen production, *J. Mater. Chem. A* 2 (2014) 3847–3855.
- [29] A. Iwase, Y.H. Ng, Y. Ishiguro, A. Kudo, R. Amal, Reduced graphene oxide as a solid-state electron mediator in Z-scheme photocatalytic water splitting under visible light, *J. Am. Chem. Soc.* 133 (2011) 11054–11057.
- [30] K. Chang, Z. Mei, T. Wang, Q. Kang, S. Ouyang, J. Ye,  $\text{MoS}_2$ /graphene cocatalyst for efficient photocatalytic  $\text{H}_2$  evolution under visible light irradiation, *ACS Nano* 8 (2014) 7078–7087.
- [31] L. Zheng, S. Han, H. Liu, P. Yu, X. Fang, Hierarchical  $\text{MoS}_2$  nanosheet@ $\text{TiO}_2$  nanotube array composites with enhanced photocatalytic and photocurrent performances, *Small* 12 (2016) 1527–1536.
- [32] B.W.H. Baugher, H.O.H. Churchill, Y. Yang, P. Jarillo-Herrero, Intrinsic electronic transport properties of high-quality monolayer and bilayer  $\text{MoS}_2$ , *Nano Lett.* 13 (2013) 4212–4216.
- [33] J. Ran, G. Gao, F.-T. Li, T.-Y. Ma, A. Du, S.-Z. Qiao,  $\text{Ti}_3\text{C}_2$  MXene co-catalyst on metal sulfide photo-absorbers for enhanced visible-light photocatalytic hydrogen production, *Nat. Commun.* 8 (2017) 13907.
- [34] X. Liu, R. Dang, W. Dong, X. Huang, J. Tang, H. Gao, G. Wang, A sandwich-like heterostructure of  $\text{TiO}_2$  nanosheets with MIL-100(Fe): a platform for efficient visible-light-driven photocatalysis, *Appl. Catal. B: Environ.* 209 (2017) 506–513.
- [35] J.M. Lee, J.L. Gunjakar, Y. Ham, I.Y. Kim, K. Domen, S.-J. Hwang, A linker-mediated self-assembly method to couple isocharged nanostructures: layered double hydroxide- $\text{CdS}$  nanohybrids with high activity for visible-light-induced  $\text{H}_2$  generation, *Chem. Eur. J.* 20 (2014) 17004–17010.
- [36] S. Chen, K. Kimura, A new strategy for the synthesis of semiconductor-metal hybrid nanocomposites: electrostatic self-assembly of nanoparticles, *Chem. Lett.* 28 (1999) 233–234.
- [37] K. Fukuda, T. Saido, J. Sato, M. Yonezawa, Y. Takasu, W. Sugimoto, Synthesis of nanosheet crystallites of ruthenate with an  $\alpha$ - $\text{NaFeO}_2$ -related structure and its electrochemical supercapacitor property, *Inorg. Chem.* 49 (2010) 4391–4393.
- [38] H.S.S. Ramakrishna Matte, A. Gomathi, A.K. Manna, D.J. Late, R. Datta, S.K. Pati, C.N.R. Rao,  $\text{MoS}_2$  and  $\text{WS}_2$  analogues of graphene, *Angew. Chem. Int. Ed.* 49 (2016) 4059–4062.
- [39] W.S. Hummers, R.E. Offeman, Preparation of graphitic oxide, *J. Am. Chem. Soc.* 80 (1958) 1339–1339.
- [40] J.-H. Choy, S.-J. Hwang, N.G. Park, Intracrystalline structure of molecular mercury halide intercalated in high- $T_c$  superconducting lattice of  $\text{Bi}_2\text{Sr}_2\text{CaCu}_2\text{O}_y$ , *J. Am. Chem. Soc.* 119 (1997) 1624–1633.
- [41] G. Kresse, J. Furthmüller, Efficiency of ab-initio total energy calculations for metals and semiconductors using a plane-wave basis set, *Comput. Mater. Sci.* 6 (1996) 15–50.
- [42] J. Perdew, K. Burke, M. Ernzerhof, Generalized gradient approximation made simple, *Phys. Rev. Lett.* 77 (1996) 3865–3868.
- [43] S. Grimme, J. Antony, S. Enrich, H. Krieg, A consistent and accurate ab initio parametrization of density functional dispersion correction (DFT-D) for the 94 elements H-Pu, *J. Chem. Phys.* 132 (2010) 154104.
- [44] A. Barnard, H. Xu, First principles and thermodynamic modeling of  $\text{CdS}$  surfaces and nanorods, *J. Phys. Chem. C* 111 (2007) 18112–18117.
- [45] D.-S. Ko, W.-J. Lee, S. Sul, C. Jung, D.-J. Yun, H.-G. Kim, W.-J. Son, J.G. Chung, D.W. Jung, S.Y. Kim, J. Kim, W. Lee, C. Kwak, J.K. Shin, J.-H. Kim, J.W. Roh, Understanding the structural, electrical, and optical properties of monolayer h-phase  $\text{RuO}_2$  nanosheets: a combined experimental and computational study, *NPG Asia Mater.* 10 (2018) 266–276.
- [46] A. Speldiani, L. Sun, Y. Zhang, T. Li, J. Kim, C.-Y. Chin, G. Galli, F. Wang, Emerging photoluminescence in monolayer  $\text{MoS}_2$ , *Nano Lett.* 10 (2010) 1271–1275.
- [47] A.K. Geim, Graphene: status and prospects, *Science* 324 (2009) 1530–1534.
- [48] Q. Lin, L. Li, S. Liang, M. Liu, J. Bi, L. Wu, Efficient synthesis of monolayer carbon nitride 2D nanosheet with tunable concentration and enhanced visible-light photocatalytic activities, *Appl. Catal. B: Environ.* 163 (2015) 135–142.
- [49] Q. Liu, Q. Shang, A. Khalil, Q. Fang, S. Chen, Q. He, T. Xiang, D. Liu, Q. Zhang, Y. Luo, L. Song, In situ integration of a metallic 1T- $\text{MoS}_2$ / $\text{CdS}$  heterostructure as a means to promote visible-light-driven photocatalytic hydrogen evolution, *ChemCatChem* 8 (2016) 2614–2619.
- [50] H. Chen, Z. Sun, S. Ye, D. Lu, P. Du, Molecular cobalt-salen complexes as novel cocatalysts for highly efficient photocatalytic hydrogen production over a  $\text{CdS}$  nanorod photosensitizer under visible light, *J. Mater. Chem. A* 3 (2015) 15729–15737.
- [51] J. Yu, S. Zhuang, X. Xu, W. Zhu, B. Feng, J. Hu, Photogenerated electron reservoir in Hetero-p-n CuO-ZnO nanocomposite device for visible-light-driven photocatalytic reduction of aqueous Cr(VI), *J. Mater. Chem. A* 3 (2015) 1199–1207.
- [52] I.Y. Kim, J.M. Lee, T.W. Kim, H.N. Kim, H.I. Kim, W. Choi, S.-J. Hwang, A strong electronic coupling between graphene nanosheets and layered titanate nanoplates: a soft-chemical route to highly porous nanocomposites with improved photocatalytic activity, *Small* 8 (2012) 1038–1048.
- [53] H.N. Kim, T.W. Kim, I.Y. Kim, S.-J. Hwang, Cocatalyst-free photocatalysts for efficient visible-light-induced  $\text{H}_2$  production: porous assemblies of  $\text{CdS}$  quantum dots and layered titanate nanosheets, *Adv. Funct. Mater.* 21 (2011) 3111–3118.
- [54] W. Lin, H. Frei, Photochemical  $\text{CO}_2$  splitting by metal-to-metal charge-transfer excitation in mesoporous  $\text{ZrCu(I)-MCM-41}$  silicate sieve, *J. Am. Chem. Soc.* 127 (2005) 1610–1611.
- [55] Z. Zhang, Y. Zhang, L. Lu, Y. Si, S. Zhang, Y. Chen, K. Dai, P. Duan, L. Duan, J. Liu, Graphitic carbon nitride nanosheet for photocatalytic hydrogen production: the impact of morphology and element composition, *Appl. Surf. Sci.* 391 (2017) 369–375.
- [56] J. Sato, H. Kato, M. Kimura, K. Fukuda, W. Sugimoto, Conductivity of ruthenate nanosheets prepared via electrostatic self-assembly: characterization of isolated single nanosheet crystallite to mono- and multilayer electrodes, *Langmuir* 26 (2010) 18049–18054.
- [57] R. Kappera, D. Voiry, S.E. Yalcin, B. Branch, G. Gupta, A.D. Mohite, M. Chhowalla, Phase-engineered low-resistance contacts for ultrathin  $\text{MoS}_2$  transistors, *Nat. Mater.* 13 (2014) 1128–1134.
- [58] H.A. Becerril, J. Mao, Z. Liu, R.M. Stoltberg, Z. Bao, Y. Chen, Evaluation of solution-processed reduced graphene oxide films as transparent conductors, *ACS Nano* 2 (2008) 463–470.
- [59] W. Li, M. Li, S. Xie, T. Zhai, M. Yu, C. Liang, X. Ouyang, X. Lu, H. Li, Y. Tong, Improving the photoelectrochemical and photocatalytic performance of  $\text{CdO}$  nanorods with  $\text{CdS}$  decoration, *CrystEngComm* 15 (2013) 4212–4216.
- [60] R. Bader, Atoms in Molecules: A Quantum Theory, Oxford Univ. Press, Oxford, 1990.
- [61] T.-H. Gu, D.A. Agyeman, S.-J. Shin, X. Jin, J.M. Lee, H. Kim, S.-J. Hwang,  $\alpha$ - $\text{MnO}_2$  nanowire-anchored highly oxidized cluster as a catalyst for  $\text{Li-O}_2$  batteries: superior electrocatalytic activity and high functionality, *Angew. Chem. Int. Ed.* 57 (2018) 15984–15989.